A radiofrequency heated reactor system for post-combustion carbon capture

Javier Fernández[a], Maria Sotenko[a], Vladimir Derevschikov[b], Anton Lysikov[b], Evgeny V. Rebrov[a,c, *]

[a] School of Engineering, University of Warwick, Coventry CV4 7AL, UK

[b] Boreskov Institute of Catalysis, pr. Lavrentieva 5, Novosibirsk, 630090, Russia

[c] Department of Biotechnology and Chemistry, Tver State Technical University, Tver 170026, Russia

* E-mail: E.Rebrov@warwick.ac.uk

Abstract

Several problems with stabilization of electricity grid system are related to the time lag between the electricity supply and demand of the end users. Many power plants run for a limited period of time to compensate for increased electricity demand during peak hours. The amount of CO_2 generated by these power installations can be substantially reduced via the development of new demand side management strategies utilizing CO_2 absorption units with a short start-up time. The sorbent can be discharged using radiofrequency (RF) heating to fill the night-time valley in electricity demand helping in the stabilization of electricity grid. Herein a concept of RF heated fixed bed reactor has been demonstrated to remove CO_2 from a flue gas using a $CaCO_3$ sorbent. A very stable and reproducible operation has been observed over twenty absorption-desorption cycles. The application of RF heating significantly reduced the transition time required for temperature excursions between the absorption and desorption cycles. The effect of flow reversal during desorption on desorption time has been investigated. The desorption time was reduced by 1.5 times in the revered flow mode and the total duration of a single absorption-desorption cycle was reduced by 20%. A reactor model describing the reduced desorption time has been developed.

Highlights

• An RF reactor system has been demonstrated for post-combustion carbon capture.

• The transition time between the absorption and desorption cycles was reduced by 2 times as compared to conventional heating

• The reverse CO_2 desorption flow mode reduced the desorption time by 1.5 times.

• The energy efficiency of RF heated and conventionally heated bench reactors was compared

1. Introduction

In 2008, the Committee on Climate Change has set up a target to reduce GHG emissions by 20 % on 1990 levels by 2020, and expected that 80-95 % reduction in total emissions would be achieved by 2050 [1]. Transport, industry & domestic heating and power plants equally contribute to the total CO_2 emissions, but because the power generation stations are large and few in numbers, whereas other sources are scattered and small, the former are considered as the better places for implementing new technologies on CO_2 mitigation in order to achieve higher efficiency and reduction potential. Depending on the used technology, a power plant could generate up to 500-800 gCO_2/kW from gas and oil and as high as 1000 g CO_2/kWh from coal [2, 3]. In 2014, the total European CO_2 emissions from power generation, 74 % of which comes from coal power stations, accounted for 1.2 billion tonnes of CO_2, whereas both China and the USA, as the main contributors, produced 5 times higher amount of CO_2 same year [2].

1.1 Carbon capture and storage technologies

There are several technologies that have been proposed to tackle the problem of CO_2 emissions: carbon capture and storage technologies [4, 5], absorption methods based on amine solutions [6] or solid minerals [7-9]. Both carbon capture & storage and solvent scrubbing towers technologies require high capital investments, whereas reverse absorption of CO_2 by freely available and cheap solid catalysts (various minerals, CaO, MgO, mixed oxides) can be considered as more commercially attractive technology. Moreover, there is a great potential for turning wastes, in this case a hot stream of effluent gases, into a feedstock for production of valuable products. For example, calcium looping cycle has been proposed for the improvement of hydrogen production in the processes of water-gas shift reaction [10] or methane steam reforming (so called sorption enhanced reforming SER) which has been verified both in fluidized [11] and fixed bed reactors [12, 13]. The large scale implication of calcium looping

cycle based on fluidized bed reactor has been proposed and economically assessed for pre- and post-combustion carbon capture [14]. It has been already used in power plants before as well [15, 16]. Another example is the combination of the carbonate looping process with the production of cement, where the raw cement meal (70 % w/w limestone, the rest are oxides of Fe, Al, Si) can be used to capture effluent CO_2 and further as the feed for clinker production [17]. Overall, the combination of the CO_2 looping with the production of other useful chemicals and materials will allow to increase energy efficiency, which is planned to be improved by 20 % from 2007 levels by 2020 as was targeted by the Committee on Climate Change [1].

Among different solid sorbents, CaO is considered to be one of the most suitable catalyst for the process of CO_2 absorption/desorption, because of its availability, low price, high durability and absorption capacity [18-23]. The reaction of CO_2 with CaO is stoichiometric and exothermic with the maximum theoretical absorption capacity of 79 wt.% [24]:

$$CaO + CO_2 \leftrightarrow CaCO_3 \quad \Delta_r H_{298}^{\circ} = -178 \text{ kJ mol}^{-1}$$
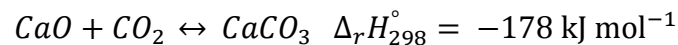
The problem of loss-in-capacity over a period of several cycles is well known phenomenon for $CaO/CaCO_3$ systems, and reported to be irrespective of the type of the initial limestone [25]. The grain size is known to have a significant effect on the sintering rate for the solid sorbents, so that smaller grains undergo faster sintering and the mechanism of the sintering has been proposed and discussed [26]. The sintering effect is profound in fluidized bed reactors, where the attrition of the catalysts particles is intensified [14], whereas in plug-flow reactors sintering could be caused by unstable heating rates and prolonged calcination times [25]. The reduction in CO_2 adsorptive capacity could be overcome by introducing to the structure of CaO some small cations, for example Al^{3+} [27] or supporting CaO on γ-alumina [28]. However, this strategy will lead to the increase in the catalysts costs.

1.2 Electricity spot price

Historically the proportion of energy usage in the form of electricity has been increasing in both developed and developing economies [29]. This inherent preference for electricity is based on its cleanliness and convenience at the point of use. This preference will only be enhanced in the future by the increasing emphasis on global sustainable energy initiatives including reduction of CO_2 emissions. Electricity spot prices differ substantially from time series of other commodities such as coal and natural gas because electricity still cannot be stored efficiently and, therefore, electricity demand has a major effect on the electricity spot price [30]. The hourly electricity spot price values are usually calculated using a volume weighted average of all trades executed through a power exchange hub and they are considered to be 24-dimensional time series [31]. The key indicator, European Energy Exchange (EEX) spot (electricity) price, fluctuates considerably during the day (Figure 1). This price is of fundamental importance as benchmark and reference point for other energy markets and these values are available via the European Energy Exchange site [32].

-- Insert Figure 1 here –

The electricity price includes a constant part caused by input costs of coal and gas and another part caused by the variations of electricity demand (Figure 1). Additional diffusion may come from the variations of the daily supply functions caused by the varying input costs.

Figure 2 shows typical costs of electricity and natural gas during a working day. It can be seen that there is a substantial period of time (between 21:00 and 07:00 next day) when the average electricity price (34 euro/MWh) is by 20% below than that of the natural gas.

-- Insert Figure 2 here --

1.3 Radiofrequency heating

The use of electromagnetic energy to selectively heat materials is well documented. For reactive systems the vast majority of research to date has focused on microwave (MW) heating. Comparatively little investigation has been conducted into the potential applications of radio frequency (RF) heating, which may be surprising given the high penetration depth and higher intrinsic safety aspects of the latter method [33]. More than 15 years ago, researchers at DuPont patented a reactor concept employing RF heating of a catalyst mesh which was used to initially ignite the chemical reaction and subsequently maintain the temperature under endothermic conditions [34]. They highlighted that such a reactor and method of operation was particularly useful for continuous production of hydrogen cyanide by the Andrussow process, a gas phase reaction operated at temperatures in excess of 1000 °C. Hydrogen cyanide was produced using an induction heated Pt group metal catalyst. The process was developed on a small scale, was highly efficient and had low installation costs [35].

Nowadays due to its high efficiency, safety and fast heating times, the RF heating technology, is increasingly being used in areas of industrial production, in metallurgy for processing of metal slabs, in civil and medical applications, such as industrial electronic encapsulation, melting technology, hypothermia, just to mention a few [36]. In general, RF heating has an efficiency of 65 to 85 % [37]. For comparison, the efficiency of conventional heating methods is about 35 to 55 %. Therefore energy savings of up to 30 % compared to conventional heating methods and up to 20-30% compared to traditional electric resistance furnace can be obtained. In addition, the RF heating process has the characteristics of easily achieving automatic control [38] and the short heating time [4]. The short heating time could lead to additional savings by 20-30% as compared to conventional heating in the low electricity demand period.

In this paper we present a concept of an RF heated tubular reactor with a CaO sorbent. Such systems can be installed for CO_2 capture at Natural Gas Combined Cycle (NGCC) power plants which are running for a limited period during each day to fulfil the maximum electricity demand. Then the sorbent can be discharged using RF heating to fill the night time valley in electricity demand (see Figure 2).

2. Methodology

2.1 Materials

A paste suitable for extrusion molding was prepared by mixing of the desired amounts of powders of CaO and nanosized polystyrene spheres with a water-ethanol mixture under vigorous stirring and grinding in a mortar. The polystyrene spheres with an average size of 180 and 800 nm were synthesized using emulsifier-free emulsion polymerization performed at 363 K as described in Sashkina et al. (2013) [39]. They were washed by ethanol and dried in air. The spheres were packed by centrifugation at a relative acceleration of 1500 rpm.

The CaO sorbent was prepared from the micron sized $CaCO_3$ powder (99 wt.%, ReaChim, Russia). The powder was calcined for 3 h at 1173 K in an oven under static air. The remaining amount of water in the samples was fixed to enable extrusion at moderate pressure while the small pieces of the paste have to keep their shape. The paste was extruded using a plunger extruder equipped with a 3 mm extrusion die. The extrudates were cut into equal parts, and obtained pellets were calcined in an oven at 1173 K for 3 h.

2.2 Lab-scale reactor set-up and operating procedures

The reactor consists of an inconel tube of 250 mm long (i.d.: 6.0 mm, o.d.: 7.0 mm, Corrotherm international). The reactor is covered by an insulating alumina tube (i.d.: 10 mm, o.d.: 16 mm, Almath crucibles). An opening with a diameter of 10 mm was made in the center of the alumina

tube for the temperature measurements. The temperature on the surface of the Inconel tube was measured with a FLIR A655sc infrared camera. In experiments with RF heating, the reactor was positioned inside a 4-turn RF coil connected to an RF- generator (Easyheat Ambrell). In conventional heating experiments, the reactor was placed in a tubular furnace.

The CaO sorbent (ca 400 mg) with a pellet size of 300-600 μm was supported onto a bed of SiC with a fraction of 300-600 which was placed on a larger SiC fraction (600-1000 μm) near the bottom. In order to support the sorbent bed, a metal rod was inserted via a T-junction at the bottom of the reactor (Figure 3).

-- Insert Figure 3 here –

The length of the supporting SiC layers was adjusted to accommodate the CaO bed in the center of the reactor. The reactor was connected to the feed line with four 3-way valves (V1, V2, V3 and V4) which allowed to operate the reactor in a by-pass mode, an absorption mode, and two desorption modes with a forward and reverse flow of N_2 relative to that in the absorption mode. The CO_2 and N_2 concentrations were continuously measured at the flow system outlet by a mass spectrometer (Pfeiffer GSD 320 O3).

In a typical experiment, the reactor was flushed with N_2 and then preheated to 938 K. The mixture of 30 vol.% CO_2 in N_2 with a flow rate of 10 mL/min (STP) was fed for analysis via a by-pass line. After temperature stabilization, the mixture was fed to the reactor and CO_2 signal was continually recorded with the mass spectrometer. During the absorption step, zero concentration of CO_2 was recorded in the outlet stream. Once the CO_2 concentration started to increase, the CO_2 flow was stopped while the N_2 flow was fed through the reactor.

In the direct flow (upstream) desorption mode, the position of three-way valves V2 and V3 remained the same, while in the reverse (downstream) desorption mode, these two valves were

switched into the opposite position to reverse the N_2 flow. Then the temperature was raised to 850°C, typically within a time interval of 30-40 s, and the CO_2 concentration was recorded in the outlet stream before starting desorption. Once the desorption cycle finishes, a new absorption cycle starts with the 30 vol. % CO_2 in N_2 mixture. Up to 20 absorption/desorption cycles have been carried out.

3. Results and discussion

3.1 Energy requirements under conventional and RF heating

Figure 4 shows the reactor temperature over multiple absorption-desorption cycles where desorption was performed without flow reversal. The feed gas entered at the bottom of the reactor and was preheated as it flowed upward in the reactor (Figure 3). During the absorption step, almost 100% CO_2 was captured from the flue gas. The absorption mode takes 20 min and the desorption mode requires 30 min. The cycle time of 57 min remains rather constant over 20 absorption/desorption cycles. It was shown earlier [22] that after sufficiently large number of cycles the CaO forms a skeleton which resists further sintering and stabilizes the capacity of the sorbent. This agrees well with the results obtained in the present study. It can be seen that RF heating allows fast and reproducible reactor heating with a very high heating rate of up to 5 K s^{-1}. RF heating can be controlled instantly and the power applied can be precisely regulated. This allows safe and precise control, even when applying very rapid heating rates. The cooling time of 180 s is slightly longer as compared to the heating time which is due to relatively low heat transfer coefficient of natural convection in this study. The cooling time can also be reduced once forced convection would be used, however this investigation was beyond the scope of the present study.

It should be noted that the transition times between the absorption and desorption modes (90 and 270 s, respectively) are much shorter as compared to the total cycle time. This is the main

advantage of RF heating mode. Despite very high heating rate, there was no overheating observed. The reduced heating time in the RF heating mode permits to reduce the total duration of the cycle by 7% and it results in reduced heat losses. A conventional heating mode using a hot air stream in a tubular furnace requires a heating time of 300 s resulting in much higher energy losses to the environment during each transition period.

-- Insert Figure 4 here –

In order to compare the energy efficiency of RF and conventional heating modes, the corresponding thermal balances were evaluated. The mean heat transfer rate to the environment (q_{RF}, Eq. 1) was estimated from gas-solid heat transfer coefficient (h_1), which, in turn, was obtained from the cooling part of the temperature profile using the equation for conservation of energy (Eq. 2). In this experiment, the reactor was heated by RF irradiation to 1173 K in the absence of gas flow. Then the heating was switched off and the cooling profile was recorded.

$$q_{RF} = \frac{h_1 A_r}{t_h} \int_0^{t_h} (T(t) - T_{ext}) \, dt \tag{1}$$

$$\Sigma_i (m_i C_{pi}) \frac{dT}{dt} = -h_1 A_r (T(t) - T_{ext}) \tag{2}$$

where m_i and C_{pi} are the weight the heat capacity of the reactor tube, sorbent and supporting layers, A_r is the external area of the reactor, t_h is the heating time T_{ext} is the temperature of the surrounding air (between the reactor and the inner wall of ceramic insulation). The obtained value of heat transfer coefficient h_1 is listed in Table 1 and the corresponding value of heat transfer rate to the environment, calculated by Eq. 1, is listed in Table 2.

It should be mentioned that at this reactor scale, the heat transfer by conduction in the porous layer is much faster than convection heat transfer. The Bi number for the RF reactor describing the convection and conduction resistances was estimated by Eq. 3

$$Bi = \frac{h_1 L}{k} \tag{3}$$

where k is effective thermal conductivity of the sorbent bed (k=4.0 W m^{-1} K^{-1}) and L is the characteristic reactor length (the ratio of the reactor volume to its surface area). Using the value for h_1 obtained from the experiment, it can be calculated that the Bi number is equal to 0.01, which justifies the absence of temperature gradients in the sorbent and the application of lumped capacitance method (Eq. 2). This result agrees well with our previous work [40] where we have shown that there is no radial temperature gradient is expected in a tubular reactor up to a diameter of 4 cm. Therefore we can conclude that there is no spacial temperature distribution inside the reactor and a single reactor temperature can be used.

-- Insert Tables 1 and 2 here –

Under RF heating, the energy is provided by volumetric heating with a volumetric heat generation rate Q''' inside the reactor with volume V. At this reactor scale, the energy needed for the heating of the process gas can be neglected as it contributes less than 5% in the total enthalpy balance. The heat released in the exothermic reaction of CO_2 absorption (0.4 W) can also be neglected as compared to the other heat fluxes as it contributes less than 1% to the overall energy balance. Thus, the reactor temperature in the RF heating mode is described by Eq. 4 using the heat capacity of the sorbent, SiC inert, and the reactor wall material [41, 42] and their respective mass fractions in the reactor.

$$\sum_i (m_i C_{pi}) \frac{dT_{RF}}{dt} = Q'''V - \underbrace{h_1 A_r (T_{RF}(t) - T_{ext,RF})}_{q_1} \qquad (4)$$

where A_r is the area of reactor and $T_{ext,RF}$ is the temperature of surrounding air inside the induction coil, m_i and C_{pi} are the weights and heat capacity of the materials, respectively. Figure 5 shows both experimental and calculated temperature profiles during RF heating. It can be seen that it takes only 90 s to increase the temperature from 926 to 1173K. A very good agreement is observed between experimental data and simulated temperature curves justifying the assumptions made.

-- Insert Figure 5 –

Under conventional heating, methane was burnt to heat up the surrounding air and then this hot air stream was used as heat transfer medium to heat up the reactor. This process can be represented by the geometry shown in Figure 6. The reactor tube is located in the middle and the methane flow is fed via parallel tubes with a smaller diameter on the shell side of the assembly. The methane is mixed with air and burnt in the shell. The methane combustion increases the temperature of the air to 1305 K during the heating step (Table 1). In this case, the reactor heating rate depends on the heat transfer rate from the hot air stream (q_2) and on the heat transfer rate to the environment (q_3) via the insulation. Here we can also neglect the heat released in the exothermic CO_2 absorption reaction and the heat needed to heat up the CO_2 and air streams. Therefore, the temperature profile in the reactor is described by Eq. 5.

$$\sum_i (m_i C_{pi}) \frac{dT_{CH}}{dt} = \underbrace{h_2 A_r (T_{hot} - T_{CH}(t))}_{q_2} - \underbrace{U_3 A_{ins} (T_{CH}(t) - T_{ext,CH})}_{q_3} \qquad (5)$$

where T_{hot} is the temperature of the hot air, h_2 is the gas-solid convection heat transfer coefficient, which was estimated from the corresponding correlation for Nu number for a tube-in-shell geometry [43], U_3 is the overall heat transfer coefficient (via insulation and adjacent gas-solid interfaces), A_{ins} is the area of insulation and $T_{ext,CH}$ is the temperature of surrounding air outside of the reactor assembly (Figure 6).

The overall heat transfer coefficient under conventional heating (U_3) was obtained by fitting the simulated by Eq. 5 curve to the experimental data (Figure 5). The corresponding value is listed in Table 1.

-- Insert Figure 6 here –

Under conventional heating, the mean heat transfer rate to the surroundings (q_{CH}), also representing the heat loss in the system, is calculated by Eq. 6.

$$q_{CH} = \frac{U_3 A_{ins}}{t_h} \int_0^{t_h} (T_{CH}(t) - T_{ext}) \, dt \qquad (6)$$

The obtained values for heat transfer rates are listed in Table 2. While the amount of energy transferred to the reactor in both cases remains near the same, it can be seen that conventional heating requires 6.5 times more energy input as compared to that under RF heating. This is mainly due to much faster heating rate which results in shorter heating time. RF irradiation is rapid and volumetric, with the whole material heated simultaneously. This feature is very important for heating of poor thermal conductors such as CaO sorbents. Under RF heating the maximum heating rate is limited by the amount of energy which can be absorbed by the medium while under conventional heating heat transfer rate q_2 is limited by temperature

13

gradient, $T_{hot} - T_{CH}$. Its maximum value depends on the reactor material and in most cases it is limited by 150 K to avoid thermal stresses. Therefore no further improvement on the heating rate under conventional heating is possible. One of the main advantages of the RF heating is that it reaches the temperature quite fast. Another advantage would be that RF heating is a green technology which involves less emissions instead of burning methane and subsequent production of more CO_2.

3.2 Effect of desorption mode

While RF heating was shown to be an effective heating mode, there is still a potential to improve the efficiency of the whole process by increasing the CO_2 desorption rate. The CO_2 desorption rate depends on the temperature, CO_2 concentration in the gas phase and internal diffusion rate inside the pellets. It is well known that the process can be performed in the kinetic regime by applying very thin sorbent layers onto structured supports [44]. Recently, the application of metal wires, gauzes and foams as support for reforming catalysts and sorbents is also considered [45]. The maximum temperature during the desorption step cannot be increased above 1173 K as this would substantially reduce the lifetime of CaO sorbent. Under these limitations, there exists only one degree of freedom in the system, which corresponds to the concentration of CO_2 along the reactor bed. It is clear that high concentration of CO_2 during desorption would results in its reabsorption in the downstream section of the bed.

To demonstrate this effect in practice, the desorption cycles have been carried out both in direct and reverse flow mode. It can be seen in Figure 7 that the sorption capacity gradually decreases after five absorption/desorption cycles and then it remains at a constant value of 15 wt.%. The sorption capacity remains the same after desorption in direct and reverse flow mode. It should be mentioned that amount of CO_2 desorbed from the sorbent during the desorption step was slightly less that the absorbed amount. The difference is due to the fact that a small portion of

CO$_2$ starts to desorb during the temperature transition step while the presented data are related to a steady state desorption at 1123 K. Additionally surface area and pore volume were analyzed for CaO before and after the reaction in ASAP2020 micromeritics (Table 3). The reduction in both of them show that there is a possible sinterisation of the catalyst used after the reaction.

-- Insert Tables 3 here –

-- Insert Figure 7 here –

Figure 8 compares two desorption modes with the direct and reverse flow modes. It can be seen that the desorption time is significantly reduced from 2000 to 1250 s in the reverse mode of operation. This phenomenon is related to different amounts of CO$_2$ absorbed in different reactor parts. The highest amount of CO$_2$ is absorbed near the reactor inlet (Eq. 11). In the direct flow desorption mode (without flow reversal), the desorption from the initial part of the bed results in CO$_2$ reabsorption in downstream locations. However after the flow reversal this part of the reactor bed becomes the outlet and the largest portion of CO$_2$ is immediately removed from the reactor with the purge gas.

-- Insert Figure 8 here –

The corresponding transient kinetic model is proposed for the reaction system (7-11). The model parameters were defined from the data obtained from transient kinetic experiments as well as from available literature data [46-48]. Following a simplified approach which does not consider the mass transfer limitations inside the pellet, the concentration of CO$_2$ in the reactor and the fraction of CO$_2$ absorbed by the sorbent (α) can be described by the following set of equations

$$\frac{\partial C_{CO2}}{\partial t} = -u\frac{\partial C_{CO2}}{\partial z} + n_t(k_d\alpha - k_aC_{CO2}(1-\alpha)) \tag{7}$$

$$\frac{\partial \alpha}{\partial t} = -k_d\alpha + k_aC_{CO2}(1-\alpha) \tag{8}$$

where k_d is the desorption constant, k_a is the absorption constant, n_A is the CO_2 absorption capacity per volume of CaO and u is the gas velocity.

The initial and boundary conditions are:

$$C_{CO2}|_{z,t=0} = 0 \tag{9}$$

$$C_{CO2}|_{z=0,t} = 0 \text{ (direct flow mode)} \tag{10a}$$

$$C_{CO2}|_{z=0.05,t} = 0 \text{ (reverse flow mode)} \tag{10b}$$

$$\alpha(z)|_{z,t=0} = 272\,z^2 - 33.6z + 1 \tag{11}$$

The actual distribution of the CO_2 fraction was approximated with a fitting function (Eq. 11). Figure 9 demonstrates an example of profiles for the CO_2 fraction within one cycle in the established cycling regime. In the direct desorption mode, the peak of maximum CO_2 concentration is moving from the inlet to outlet (Figure 9a). Due to reversible CO_2 absorption, a considerable amount of CO_2 is still present near the reactor outlet after 1800s. However after the flow reversal (Figure 9b), the inlet part of the catalyst bed becomes the outlet one and the area of CO_2 accumulation appears at the reactor outlet. In the beginning of the cycle, the CO_2 concentration here is the highest due to the highest desorption rate. Thus the total desorption a time is reduced from 35 min to 20 min in the reverse flow mode. This allows to reduce the total cycle duration by 20%. It should be mentioned that the simulation results are in a good

agreement with experimental data under the assumptions of constant bed temperature and the absence of mass transfer limitations.

-- Insert Figure 9 here –

Knowing the time of desorption in each mode, it can be concluded that the energy input in the direct mode (Eq. 1) is 1.5 times higher than that in the reverse desorption mode.

As for the possible scale up for this process, it potentially depends on the power required for the application. In the carried out experiments, the power was less than 1 kW as this is the maximum of the RF generator. Typical industrial providers for induction heating such as Ambrell and EFD have indicated that the normal requirements for industrial cases are between 50 – 100 kW and they are totally feasible for industrial applications which is two orders more than in our laboratory case. Furthermore RF heating has been previously studied as a doable alternative in the scale-up for industrial applications in pharmacy or fine chemistry [40]. In this case of CO_2 absorption/desorption cycles, depending on the diameter of the Inconel tube in the scale-up, radial temperature distribution could be observed, but anyway RF heating would have the maximum on the wall, so it would be worth studying it.

Conclusions

For the first time, CO_2 capture performance of a radiofrequency heated reactor with a CaO sorbent was evaluated. By rapidly shifting from absorption to desorption through over 20 cycles with a mixture containing 30 vol.% CO_2 in nitrogen, the sorbent has demonstrated a very stable performance, exhibiting high CO_2 absorption efficiency over 99.9%. Similar CO_2 absorption efficiency was obtained under conventional heating mode, however the latter resulted in 9 times higher heat losses to the environment during the heating step. The transition time between

the CO_2 absorption and desorption modes was reduced by a factor of three using RF heating. The application of RF heating provided substantial energy savings as it drastically reduces the reactor idle time at high temperatures.

The CO_2 desorption in a reverse flow mode further reduced the cycle time by 20% as it decreased the CO_2 partial pressure over the adsorbent that substantially prevented CO_2 reabsorbtion. The reverse flow mode also allowed to obtain a higher CO_2 concentration in the purge gas the than that in the feed. This creates a possibility to use hydrogen as purge gas that would create a mixture suitable for methanol synthesis.

Acknowledgements

Nomenclature

A_{ins}	external area of insulation (m^2)
A_r	external area of reactor (m^2)
C_{CO2}	CO$_2$ concentration (mol m^{-3})
$\bar{C}$	average CO$_2$ concentration (mol m^{-3})
C_p	heat capacity (J kg^{-1} K^{-1})
E_a	activation energy (J mol^{-1})
F_V	volumetric flow of gas (m^3 s^{-1})
ΔH_h	heating enthalpy, $\Delta H = \sum_i (m_i C_{pi})\Delta T + \sum_j (\dot{m}_j C_{pj}) t_h \Delta T$ (J)
h_1	gas-solid heat transfer coefficient from the reactor to the surrounding air (W m^{-2} K^{-1})
h_2	gas-solid heat transfer coefficient of forced convection around a cylinder (W m^{-2} K^{-1})
k_a	absorption rate constant (m^3 mol^{-1} s^{-1})
k_d	desorption rate constant (s^{-1})
m	weight (kg)
$\dot{m}$	mass flow rate (kg s^{-1})
n	amount of CO$_2$ absorbed per volume of sorbent (mol m^{-3})
n_{max}	maximum amount of CO$_2$ absorbed per volume of sorbent (mol m^{-3})
$\bar{n}$	average amount of CO$_2$ absorbed per volume of sorbent (mol m^{-3})
q	heat transfer rate (W)
t	time (s)
T	temperature (K)
ΔT	temperature difference, $\Delta T = T_d - T_a$ (K)
u	gas superficial velocity (m s^{-1})

U_3 overall heat transfer coefficient (W m^{-2} K^{-1})

V_R volume of sorbent (m^3)

z   reactor axial coordinate (m)

Greek letters

α fraction of CO_2 absorbed, $\alpha = \dfrac{n}{n_{max}}$ (-)

ε bed porosity (-)

Subscripts

1   heat transfer from the reactor wall to the surrounding air

2   heat transfer from the hot air stream to the reactor

3   heat transfer from the reactor via insulation to the surrounding air

a   absorption

CH   conventional heating

d   desorption

ext   external

h   heating

hot   hot air

i   solid component index (sorbent, inert, Inconel)

j   fluid component index (CO_2, N_2)

RF   RF heating

Figure captions

Figure 1.   Time series of electricity demand (top panel) corresponding electricity spot prices (bottom panel) over 5 work days (January 12-16, 2015) [32].

Figure 2.   Daily electricity spot price and natural gas EPEX day price (January 15, 2015).

Figure 3.   (a) Schematic view of the reactor, (b) Piping flow diagram.

Figure 4.   Temperature profile during multiple absorption-desorption cycles under RF heating.

Figure 5.   Conventional and radiofrequency heating. Experimental data are shown with symbols. The simulations with Eq. 4 (T_{RF}) and Eq. 5 (T_{CH}) are shown with solid lines.

Figure 6.   A schematic view of conventional heating mode and corresponding heat transfer rates.

Figure 7. CO_2 sorption capacity in absorption and two desorption modes with direct and reverse flow.

Figure 8. CO_2 concentration at the reactor outlet in the direct and reverse flow desorption modes. Temperature: 1123 K. Flow rate: 0.117 $cm^3 s^{-1}$ (STP).

Figure 9.   Profiles for the CO_2 fraction as a function of reactor coordinate within one desorption cycle in the established cycling regime. (a) Direct flow and (b) reverse flow mode. Reaction conditions are the same as those in Figure 8. The flow direction is shown with an arrow.

Tables

Table 1. Reactor parameters and process conditions

Parameter	Value
A_r (m^2)	$9.42 \cdot 10^{-4}$
A_{ins} (m^2)	$3.14 \cdot 10^{-3}$
h_1 (W m^{-1} K^{-1})	29
h_2 (W m^{-1} K^{-1})	32
U_3 (W m^{-1} K^{-1})	2.1
C_{p-CaO} (J kg^{-1} K^{-1})	940
C_{p-SiC} (J kg^{-1} K^{-1})	850
C_{p-INC} (J kg^{-1} K^{-1})	450
T_h (K)	1305
$T_{ext,RF}$ (K)	620

Table 2. Enthalpy change and mean heat transfer rate to the environment during reactor heating from 926 to 1123K

Parameter	RF heating	Conventional heating
q (W)[a]	5.5	19.7
Total enthalpy change, ΔH (kJ)	1.3	10.3
Heating enthalpy, ΔH_h (kJ)	0.2	0.2
ΔH_{loss} (kJ)	1.1	10.1

[a] calculated by Eqs. 1 and 6, respectively

Table 3. Surface area, pore volume and average pore size for CaO before and after the reaction.

Sorbent	Surface area (m^2/g)	Pore volume (cm^3/g)
CaO fresh	28.61	0.045
CaO used	13.05	0.021

References

[1]   T.C.o.C. Change, Climate Change Act 2008. 2008;Chapter 27:1-103

[2]   Olivier J.G.J., Janssens-Maenhout G., Muntean M.Peters J.A.H.W., Trends in global CO_2 emissions: 2014 Report. 2014, PBL Netherlands Environmental Assessment Agency: The Hague, Netherlands. p. 1-60.

[3]   McIntyre J., Berg B., Seto H.Borchardt S., WNA report: Comparison of Lifecycle Greenhouse Gas Emissions of Various Electricity Generation Sources. 2010, World Nuclear Association: London, UK. p. 1-12.

[4]   Anderson S.Newell R., Prospects for Carbon Capture and Storage Technologies. Discussion paper 2003:1-67.

[5]   Golombek R., Greaker M., Kittelsen S.A.C., Røgeberg O.Aune F.R., Carbon capture and storage technologies in the European power market. Discussion Papers No. 603 2009:1-29.

[6]   Dutcher B., Fan M.Russell A.G., Amine-Based CO_2 Capture Technology Development from the Beginning of 2013: A Review. ACS Appl Mater Inter 2015; 4:2137-48.

[7]   Dou B., Wang C., Song Y., Chen H., Jiang B., Yang M.YujieXu, Solid sorbents for in-situ CO_2 removal during sorption-enhanced steam reforming process: A review. Renew Sust Energ Rev 2016; 53:536–546.

[8]   Bhatta L.K.G., Subramanyam S., Chengala M.D., Olivera S.Venkatesh K., Progress in hydrotalcite like compounds and metal-based oxides for CO_2 capture: a review. Jof Clean Prod 2015; 103:171-196.

[9]   Samanta A., Zhao A., Shimizu G.K.H., Sarkar P., Gupta R.,Bhatta L.K.G., Post-combustion CO_2 capture using solid sorbents: A review. Ind Eng Chem Res 2011;51:1438-1463.

[10] Symonds R.T., Lu D.Y., Hughes R.W., Anthony E.J.Macchi A., CO_2 Capture from Simulated Syngas via Cyclic Carbonation/Calcination for a Naturally Occurring Limestone: Pilot-Plant Testing. Ind Eng Chem Res 2009; 48:8431–8440.

[11] Chen Z., Grace J.R. Lim C.J., CO_2 Capture and Hydrogen Production in an Integrated Fluidized Bed Reformer-Regenerator System. Ind Eng Chem Res 2011; 50:4716–4721.

[12] Cobden P.D., Elzinga G.D., Booneveld S., Dijkstra J.W., Jansen D.Brink R.W.v.d., Sorption-enhanced steam-methane reforming: CaO-$CaCO_3$ Capture technology. Energy Procedia 2009; 1:733–739.

[13] Garcıa-Lario A.L., Aznar M., Martinez I., Grasa G.S. Murillo R., Experimental study of the application of a $NiO/NiAl_2O_4$ catalyst and a CaO-based synthetic sorbent on the Sorption Enhanced Reforming process. Int J Hydrogen Energ 2015; 40:219-232.

[14] Blamey J., Anthony E.J., Wang J., Fennell P.S., The calcium looping cycle for large-scale CO_2 capture. Progress in Energy and Combustion Science 2010; 36:260–279.

[15] Romeo L.M., Lara Y., Lisbona P., Martinez A., Economical assesment of competitive enhanced limestones for CO2 capture cycles in power plants. Fuel ProcessTechnol 2009; 90:803-811.

[16] Ortiz C., Chacartegui R., Valverde J.M., Becerra J.A., A new integration model for calcium looping technology into coal fired power plants for CO2 capture. Appl Energy 2016; 169:408-420.

[17] Pathi S.K., Lin W., Illerup J.B., Dam-Johansen K., Hjuler K., CO_2 Capture by Cement Raw Meal. Energ Fuel 2013; 27:5397−5406.

[18] Udomsirichakorn J., Salam P.A., Review of hydrogen-enriched gas production from steam gasification of biomass: The prospect of CaO-based chemical looping gasification. Renew Sust Energ Rev 2014; 30:565–579.

[19]   Sánchez-Biezma A., Ballesteros J.C., Diaz L., Zárraga E.d., Álvarez F.J., López J., Arias B., Grasa G., Abanades J.C., Postcombustion CO_2 capture with CaO. Status of the technology and next steps towards large scale demonstration. Energy Procedia 2011; 4:852–859.

[20]   Yancheshmeh M.S., Radfarnia H.R., Iliuta M.C., High temperature CO_2 sorbents and their application for hydrogen production by sorption enhanced steam reforming process. Chem Eng J 2016; 283:420–444.

[21]   Felice L.D., CO_2 Capture by CaO-Based Sorbents and Sorption Enhanced Reaction Systems, in Activation of Carbon Dioxide. 2013, Elsevier. p. 603-624.

[22]   Derevschikov V.S., Lysikov A.I., Okunev A.G., Sorption properties of lithium carbonate doped CaO and its performance in sorption enhanced methane reforming. Chem Eng Sci 2011; 66:3030–3038.

[23]   Lysikov A.I., Trukhan S.N., Okunev A.G., Sorption enhanced hydrocarbons reforming for fuel cell powered generators. Int J Hydrogen Energ 2008; 33:3061 – 3066.

[24]   Lysikov A., Derevschikov V., Okunev A., Sorption-enhanced reforming of bioethanol in dual fixed bed reactor for continuous hydrogen production. Int J Hydrogen Energ 2015; in press.

[25]   Grasa G.S., Abanades J.C., CO_2 Capture Capacity of CaO in Long Series of Carbonation/Calcination Cycles. Ind Eng Chem Res 2006; 45:8846-8851.

[26]   Lysikov A.I., Salanov A.N., Okunev A.G., Change of CO_2 Carrying Capacity of CaO in Isothermal Recarbonation-Decomposition Cycles. Ind Eng Chem Res 2007; 46:4633-4638.

[27]   Beruto D.T., Botter R., Lagazzo A., Finocchio E., Calcium oxides for CO_2 capture

obtained from the thermal decomposition of $CaCO_3$ particles coprecipitated with Al^{3+}

ions. J Eur Cera Soc 2012; 32:307–315.

[28]   Feng B., Liu W., Li X., An H., Overcoming the Problem of Loss-in-Capacity of

Calcium Oxide in CO_2 Capture. Energ Fuel 2006; 20:2417-2420.

[29]   Kumar R., Ray P.D., Reed C. Smart grid: An electricity market perspective. in

Innovative Smart Grid Technologies (ISGT), 2011.

[30]   Knittel C.R., Roberts M.R., An empirical examination of restructured electricity

prices. Energ Econ 2005; 27:791-817.

[31]   Koopman S.J., Ooms M., Carnero M.A., Periodic seasonal Reg-ARFIMA–GARCH

models for daily electricity spot prices. J Am Stat Assoc 2007; 102:16-27.

[32]   www.eex.com. 2015.

[33]   Chatterjee S., Degirmenci V., Rebrov E.V., Design and operation of a radio-frequency

heated micro-trickle bed reactor for consecutive catalytic reactions. Chem Eng J 281

(2015) 884–891 2015; 281:884–891.

[34]   Krause K.R., Catalytic oxidation of volatile carbon compounds into carbon monoxide

using induction heating. 1997, E. I. Du Pont de Nemours & Co., USA . p. 4 pp., Cont.

of U. S. Ser. No. 440,958.

[35]   Kreutzer K.A., Tam W., Hydrocyanation process and multidentate phosphite and

nickel catalyst composition therefor. 1996, Google Patents.

[36]   Liu W., Chen M., Xi Y., Lin C., Liu S. Thermo-mechanical analysis of a wafer level

packaging by induction heating. in Electronic Packaging Technology & High Density

Packaging, 2008. ICEPT-HDP 2008. International Conference on. 2008. IEEE.

[37]   Tavakoli M.H., Karbaschi H., Samavat F., Influence of workpiece height on the

induction heating process. Math Comput Model 2011; 54:50-58.

[38]   Bodart O., Boureau A.-V., Touzani R., Numerical investigation of optimal control of induction heating processes. Appl Math Model 2001; 25:697-712.

[39]   Sashkina K., Labko V., Rudina N., Parmon V., Parkhomchuk E., Hierarchical zeolite FeZSM-5 as a heterogeneous Fenton-type catalyst. J. Catal 2013; 299:44-52.

[40]   Fernández J., Chatterjee S., Degirmenci V., Rebrov E.V. Scale-up of an RF heated micro trickle bed reactor to a kg/day production scale, Green Process Synth 2015; 4: 343–353.

[41]   Leitner J., Chuchvalec P., Sedmidubský D., Strejc A., Abrman P., Estimation of heat capacities of solid mixed oxides. Thermochim acta 2002; 395:27-46.

[42]   Perry J.H., Chemical engineers' handbook. J. Chemical Education. Vol. 27. 1950.

[43]   Bejan A., Convection heat transfer,4th Edition, Wiley, 2013.

[44]   Derevschikov V.S.,Veselovskaya, J.V., Kardash, T.Y., Trubitsyn, D.A., Okunev, A.G, Direct CO_2 capture from ambient air using K_2CO_3/Y_2O_3 composite sorbent. Fuel 2014; 127: 212-218.

[45]   Sang, L., Sun B., Tan H., Du C., Wu Y., Ma C., Catalytic reforming of methane with CO_2 over metal foam based monolithic catalysts. Int. J. Hydrogen Energy 2012; 37: 13037-13043.

[46]   Lee D.K., An apparent kinetic model for the carbonation of calcium oxide by carbon dioxide. Chem Eng J 2004; 100:71-77.

[47]   Yu Y.S., Liu W.Q., An H., Yang F.S., Wang G.X., Feng B., Zhang Z.X., Rudolph V., Modeling of the carbonation behavior of a calcium based sorbent for CO_2 capture. Int J Greenh Gas Con 2012; 10:510-519.

[48]   Zhou Z., Xu P., Xie M., Cheng Z., Yuan W., Modeling of the carbonation kinetics of a synthetic CaO-based sorbent. Chem Eng Sci 2013; 95:283-290.
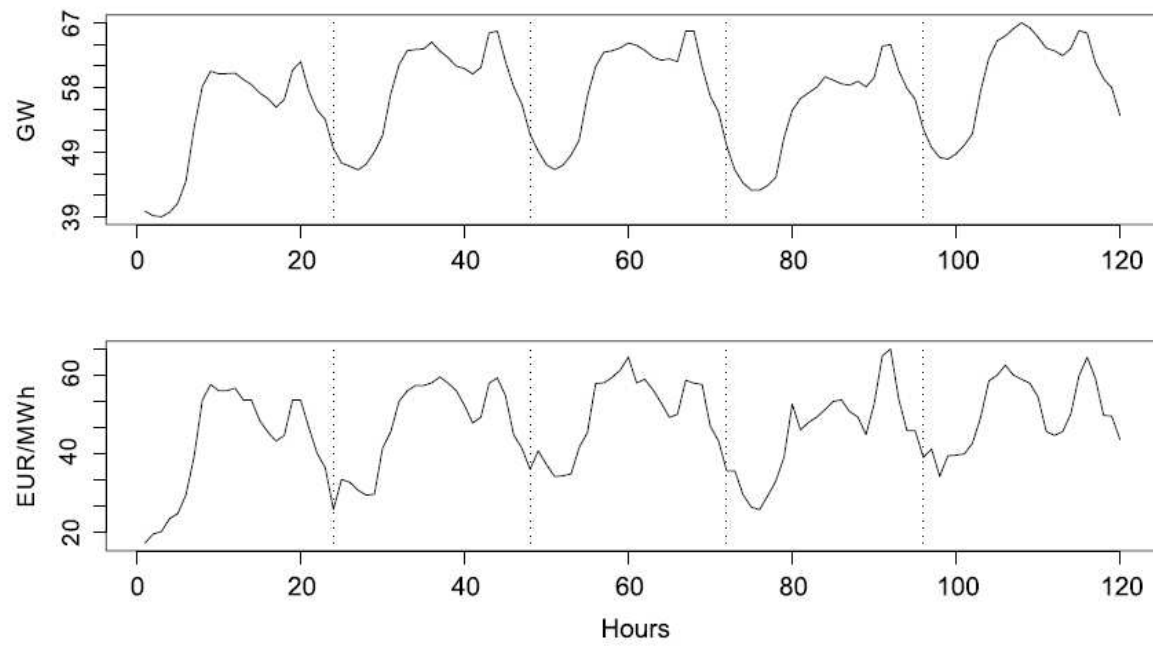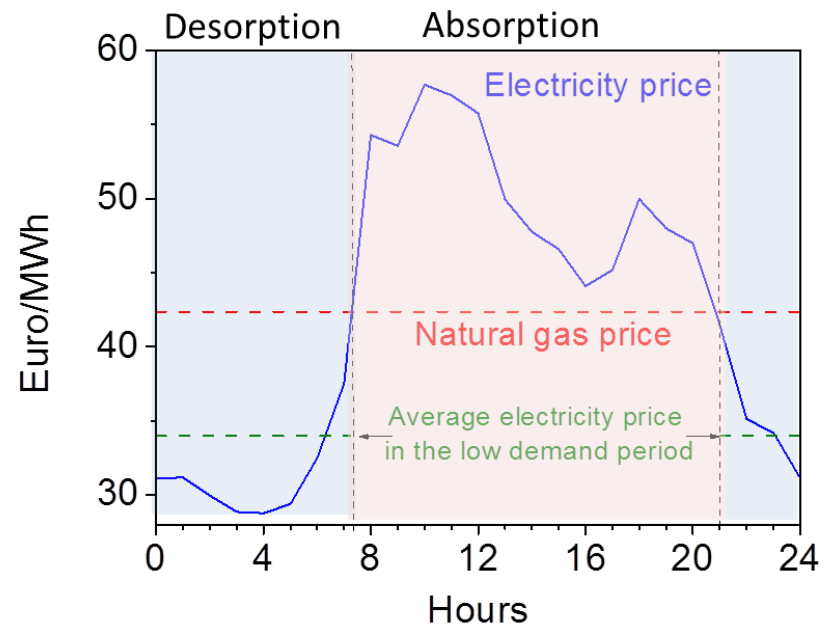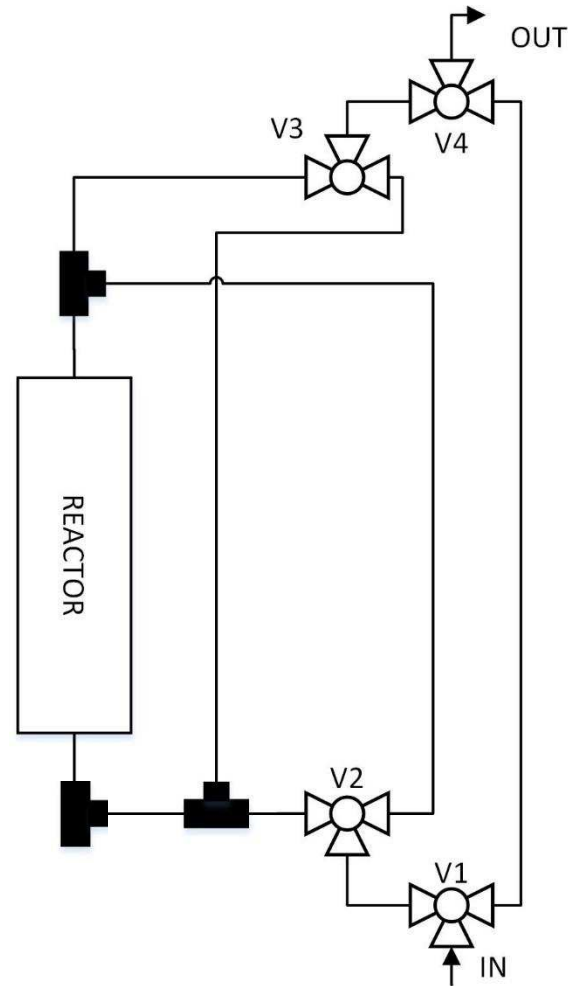
Figure 1

Figure 2

(a)

(b)

OUT

V3   V4

REACTOR

V2

V1

IN
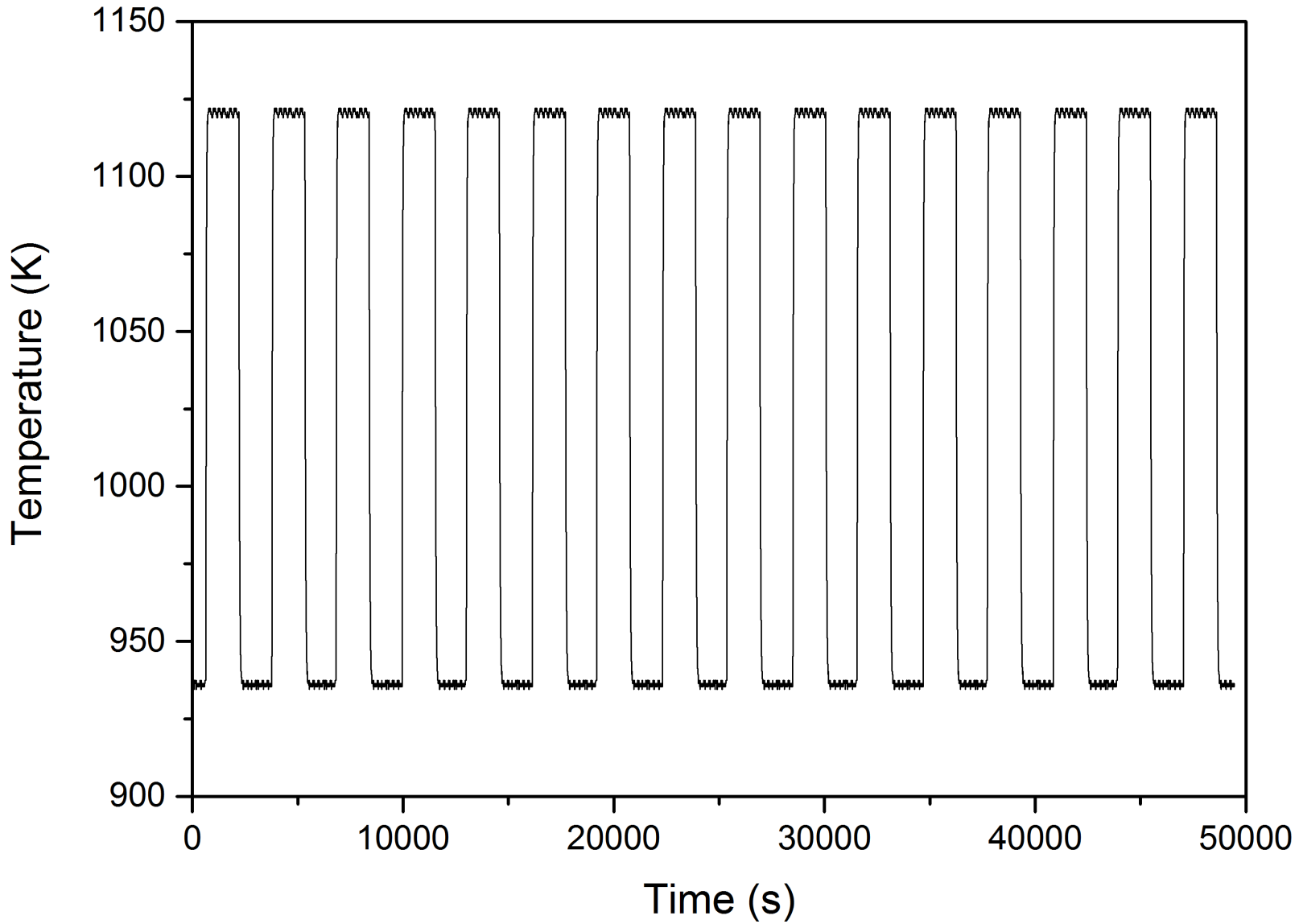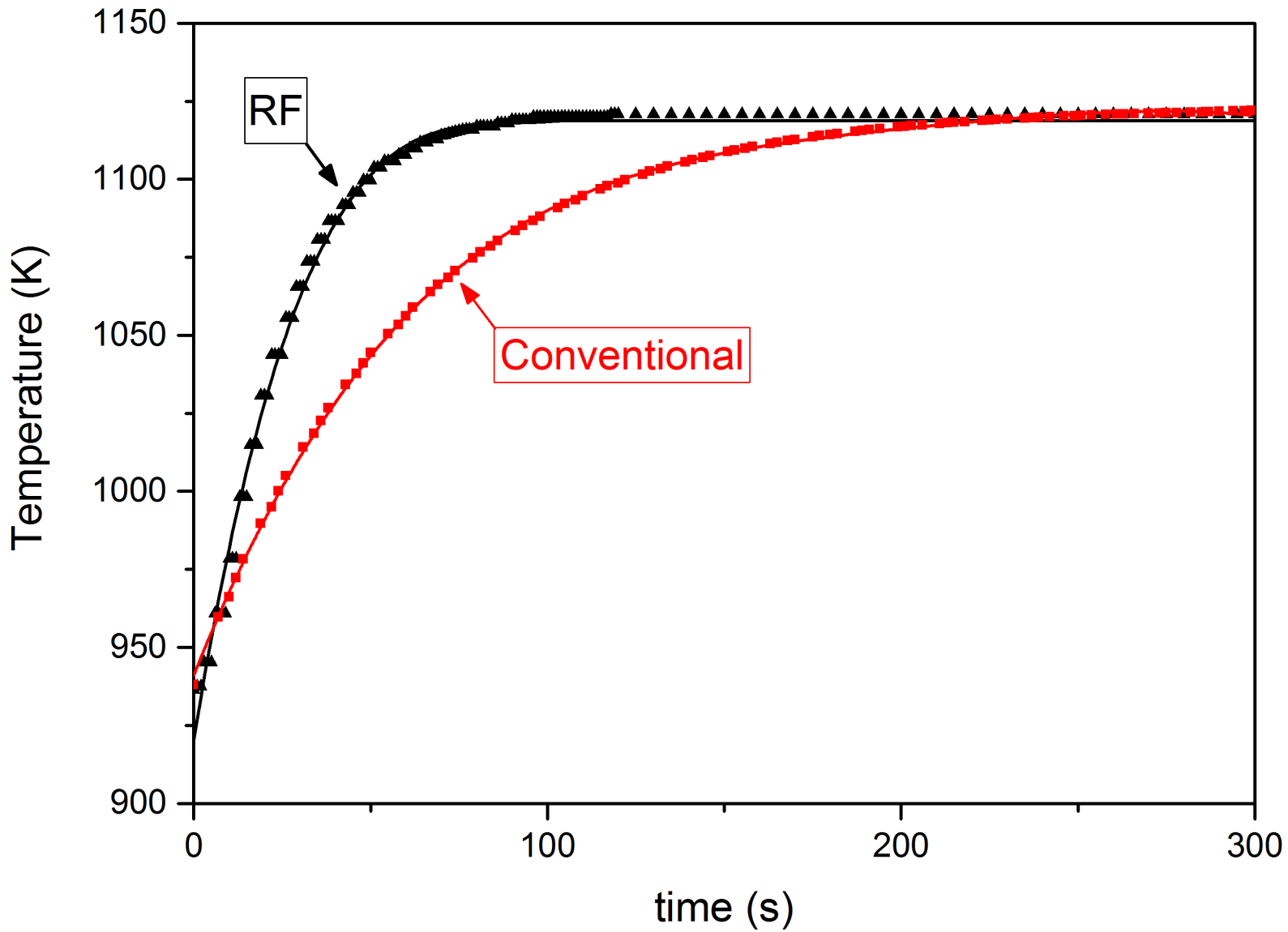
Figure 3

Figure 4

Figure 5
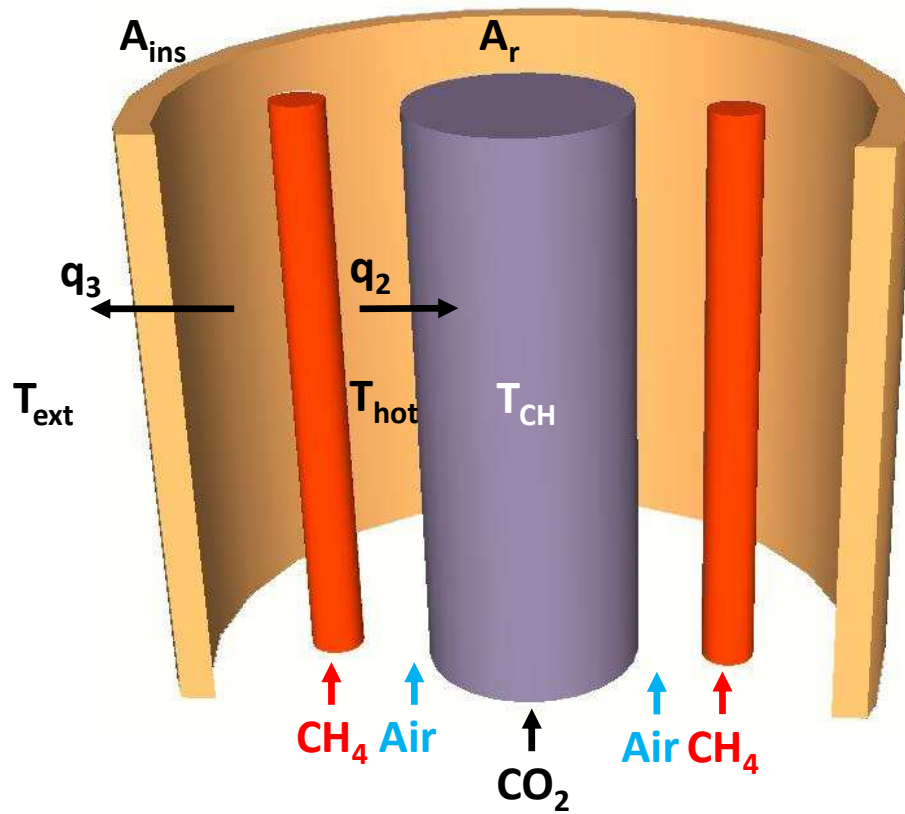
Figure 6

Figure 7

Figure 8

Figure 9